Available online at www.sciencedirect.com

ScienceDirect

Acta Materialia 83 (2015) 256–268

Acta MATERIALIA

www.elsevier.com/locate/actamat

Cyclic behaviour of a 6061 aluminium alloy: Coupling precipitation and elastoplastic modelling

D. Bardel,[a,b,c] M. Perez,[b,*] D. Nelias,[a] S. Dancette,[b] P. Chaudet[a] and V. Massardier[b]

[a] *Université de Lyon, INSA-Lyon, LaMCoS UMR CNRS 5259, F69621 Villeurbanne, France*
[b] *Université de Lyon, INSA-Lyon, MATEIS UMR CNRS 5510, F69621 Villeurbanne, France*
[c] *AREVA NP, Département d'ingénierie mécanique, Lyon, France*

Received 1 August 2014; revised 5 September 2014; accepted 5 September 2014

Abstract—Multi-level cyclic loading is performed on an aluminium 6061 alloy. From an initial fully precipitated T6 state, various non-isothermal heat treatments are performed, leading to various precipitation states. This paper focuses on the effect of precipitates on yield stress, and on kinematic and isotropic hardening. In parallel, the elastoplastic behaviour is modelled coupling a recently developed multi-class precipitation model to an adaptation of the classical Kocks–Mecking–Estrin formalism. In addition to the classical isotropic effect of solid solution, precipitates and dislocation forests, the proposed model takes into account the kinematic contribution of grain boundaries as well as precipitates, thus providing a new physical meaning to the Armstrong–Frederick law. The resulting cyclic stress–strain curves compare well with the experimental ones for all treatments and strain levels.

Keywords: Isotropic hardening; Kinematic hardening; Precipitation; Age hardening; Cyclic loading

1. Introduction

Understanding of the microstructural evolutions and associated deformation mechanisms in age-hardening aluminium alloys has greatly progressed in the last decade (see for example the recent review of Simar et al. [1]). In their pioneering contribution, Myhr et al. [2,3] coupled a Kampmann–Wagner numerical (KWN) precipitation model with a dislocation strengthening model in 6XXX alloys after non-isothermal heat treatments, typical of that used for welding. The aim of this kind of studies is generally to predict yield stress, hardness [2,4,5] and, sometimes, strain hardening during a tensile test [1,6]. Nevertheless, despite this progress, the literature is more sparse on the cyclic behaviour of 6XXX alloys, for which accurate constitutive laws are needed for several applications such as fatigue or welding (especially for multi-pass processes).

Beyond practical applications, the use of cyclic behaviour enables some limitations attached with monotonous testing to be overcome. For example, kinematic hardening can be erroneously attributed to isotropic mechanisms, based on monotonous loading. The use of cyclic loading is then fundamental to separate the kinematic and isotropic contributions and thus better understand the hardening behaviour of age-hardening alloys.

In the literature, several authors have studied the impact of microstructural evolutions on the kinematic hardening of age-hardening aluminium alloys. Proudhon et al. [7] investigated the Bauschinger effect induced by isothermal treatments and proposed some elements of kinematic hardening modelling inspired by the pioneer contributions of Ashby [8], Brown and Stobbs [9]. Later, several teams took over these early studies: e.g. Fribourg et al. [10] on 7XXX series, and Teixeira et al. [11] and Han et al. [12] for Al–Cu–Sn alloys. However, these papers share a common drawback: the entire kinematic hardening is attributed to the precipitates, thus neglecting the potential impact of grain boundaries (as studied by Sinclair et al. [13]).

In this study a cyclic elastoplastic model is coupled to a recently developed precipitation model [14]. This coupling aims at understanding and describing the variety of cyclic behaviour that can be encountered in the heat-affected zone of a 6061-T6 weld joint. The modelling approach is based on:

- a robust precipitation model (KWN-type) detailed in previous papers [15,16] that has been recently adapted for rod-shaped precipitates and validated by transmission electron Microscopy (TEM) as well as small-angle neutron scattering (SANS) [14],
- an isotropic hardening model based on the Kocks–Mecking–Estrin (KME) formalism [17–19] embellished by the consideration of the entire precipitate

* Corresponding author; e-mail addresses: michel.perez@insa-lyon.fr; daniel.nelias@insa-lyon.fr

http://dx.doi.org/10.1016/j.actamat.2014.09.034
1359-6462/

Nomenclature

b	Burgers vector
C^{AF}	constant of the Armstrong–Frederick model
D	grain size
E	Young's modulus
f	yield surface
f_V	volume fraction of the β'' – β' hardening phase
f_V^{bp}	volume fraction of bypassed precipitates
i_c	index of the class corresponding to the transition radius
k	strength constant for precipitate shearing calculation
k_1	multiplication constant in the KME model
k_2^0, k_2^p	dynamic recovery coefficients in the KME model
k_j	solid-solution strengthening constant for element "j"
$\overline{L_{bp}}$	mean distance between bypassed precipitates
l_i	length of the precipitate rod in the class "i"
l_{bp}	mean length of bypassed precipitates
M	Taylor factor
N_i	precipitate density in the class "i"
n_G	number of dislocation stored at grain boundaries
n_G^*	maximum number of dislocation stored at grain boundaries
n_{ppt}	number of dislocations stored around precipitates
n_{ppt}^*	maximum number of dislocations stored around precipitates
R	total isotropic hardening coefficient
$\overline{R}$	mean radius of the precipitate distribution
$\overline{R_{bp}}$	mean radius of the bypassed distribution
r^c	transition radius between sheared and bypassed precipitates
S_{ijkl}	component "$ijkl$" of the Eshelby tensor S
X_G	kinematic stress due to grain boundaries
X_{ppt}	kinematic stress due to Orowan storage
α	constant related to the forest hardening
β	constant related to dislocation line tension
γ^{AF}	constant of the Armstrong–Frederick model
$\Delta\sigma^{bp}$	bypassed precipitate contribution to strength
$\Delta\sigma_p$	precipitate contribution to strength
$\Delta\sigma^{sh}$	sheared precipitate contribution to strength
$\Delta\sigma_{SS}$	solid-solution contribution to strength
ϵ	uniaxial total strain
ϵ_e	elastic part of the strain
ϵ_p	uniaxial plastic strain
ϵ_p^*	unrelaxed plastic strain
κ	ratio of the length of the precipitate by its diameter
$\dot{\lambda}$	plastic multiplier
λ_G	mean spacing between slip lines at grain boundaries
μ	Shear modulus of the matrix
μ^*	shear modulus of the precipitates
ν	Poisson coefficient
ξ	effective stress ($\xi = \sigma - X_G - X_{ppt}$)
Ω	Brown and Stobbs accommodation factor
φ	efficiency parameter for Orowan storage ($\in [0, 1]$)
ρ	dislocation density statistically stored
ρ_0	initial dislocation density
ρ_{ppt}	dislocation density stored in form of Orowan loops
σ_0	pure aluminium yield stress
$\sigma_{0.02\%}^y$	yield stress for 0.02% of plastic strain
χ	constant in X_{ppt} expression

distribution, solid-solution strengthening (as presented in Ref. [14]) as well as a precipitate-induced recovery mechanism [6],
- a kinematic hardening model based on grain and precipitate contributions, adapted from the work of Sinclair et al. [13], Brown and Stobbs [9] and Proudhon et al. [7] for cyclic hardening.

This approach will be validated by uniaxial multilevel cyclic loadings performed on specimens that were subjected beforehand to non-isothermal heat treatments, representative of welding thermal histories in a heat-affected zone as in Ref. [14]. The slip irreversibility mentioned in Ref. [12] is assumed negligible in this work, which simplifies the treatment of isotropic and kinematic contributions to the hardening. We indeed believe here that a clear description of slip irreversibility should come after a proper description of isotropic and kinematic effects, on which this paper is focused.

2. Materials and experimental methods

2.1. Materials and heat treatments

Uniaxial specimens were extracted from a 6061-T6 rolled plate of 50 mm thickness. The alloy composition is given in Table 1. In order to mimic the thermal cycles occurring in a heat-affected zone, two kinds of controlled heating cycles were performed on a home-made Joule thermomechanical simulator presented in Ref. [20] and improved for this study. Each cycle was composed of a heating stage (at constant heating rate) up to a maximum temperature, followed by natural cooling, as in the welding process (cooling rate between 30 and 50 °C s^{-1} depending on treatment). The specimen dilatation and contraction was free during these thermal cycles. In order to study the effect of both heating rate and maximal temperature, two types of treatments will be presented as detailed in Ref. [14]:

Table 1. Chemical composition of studied AA6061 (main elements).

	Mg	Si	Cu	Fe	Mn	Cr	Zn
wt.%	1.02	0.75	0.25	0.45	0.06	0.06	0.04
at.%	1.14	0.72	0.11	0.22	0.03	0.03	0.02

- "*Maximum temperature*" *(MT) treatments*: at a fixed heating rate close to 15 °C s^{-1}, maximum temperatures from 100 to 560 °C were reached;
- "*Heating rate*" *(HR) treatments*: at a fixed maximum temperature (400 °C), heating rates from 0.5 to 180 °C s^{-1} were experienced.

Temperatures were measured with a Micro-Epsilon CT laser pyrometer (9 ms response time, 8–14 μm wavelength) focused on the samples, which were coated with a thin graphite film of known emissivity. This device was linked to a MTS teststarS IIm controller of the tensile machine (response time 10 ms) and used to obtain accurate temperature measurements and improve the thermal regulation presented in Ref. [20] (no overshooting with an accuracy of ±2 °C). For *MT* treatments, the temperatures were 100, 300, 400, 450, 500 and 560 °C (experimental heating rate was 14.6 °C s^{-1} ±0.1). *HR* treatments were performed with heating rates of 0.48, 14.7, 69.5 and 181 °C s^{-1} for a maximum temperature of 400 °C. It is assumed here that these fast treatments do not impact the grain structure and size.

2.2. Cyclic loading and specimen design

The Joule device was attached to a MTS-809 tensile machine (100 kN load cell) in order to load the samples directly after the heat treatment. This avoided natural aging [21] for samples heated to 500–560 °C (where all the hardening β'' – β' precipitates were dissolved [14]) and air quenched.

In order to avoid buckling of the specimens and to achieve fast heating rates, we chose to limit the strain to less than 1% (cf. Fig. 1) with a reduced diameter (7.05 mm). The samples have been designed using analytical estimates as well as electrothermal finite-element method (FEM) simulations performed with the commercial software Abaqus. The length has been chosen as a compromise between the risk of buckling for 1% strain and temperature gradient. Thanks to a spacing modification on a biaxial MTS extensometer as in Ref. [22] (cf. Fig. 2), the gage length was reduced to 15 mm. The temperature gradient in this area has been checked by a thermographic camera FLIR SC7750L 8–9.4 μm (cf. Fig. 2). A variation of 6% at 7.5 mm from the center was obtained for the highest temperature.

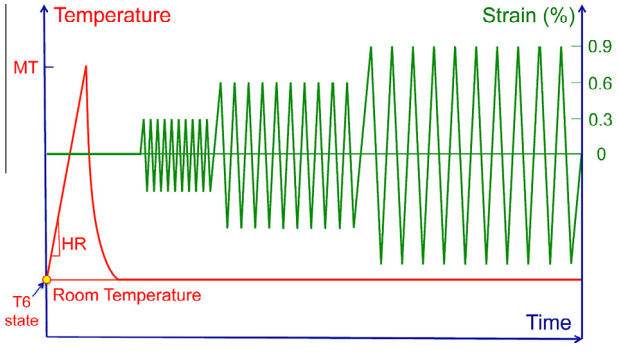

Fig. 1. From the T6 initial state, thermomechanical treatments are performed. First, non-isothermal heat treatments characterized by a heating rate (HR) and a maximum temperature (MT) are performed. Then, three sets of 10 cycles with increasing strain (0.3, 0.6 and 0.9%) are performed at room temperature.

Multilevel strain cycles have been performed, consisting of three sets of 10 cycles with increasing amplitude (cf. Fig. 1). Indeed, isotropic and kinematic hardening contributions are known to depend on the plastic strain amplitude ϵ_p (uniaxial here) but also on the cumulative plastic strain p such as $\dot{p} = |\dot{\epsilon_p}|$ for a large range of materials [23]. Moreover, as we will see later, this type of test allows an easy estimation of both hardening components separately. For the T6-treated sample, MT treatments with $MT = 100$ °C and $MT = 300$ °C specimens, the stress was rapidly stabilized, so that the tests were shortened.

2.3. Transmission electron microscopy

TEM experiments were conducted on a 200CX microscope operating at 200 kV, belonging to the Centre Lyonnais de Microscopie (CLYM) located at INSA Lyon (France). The samples used for TEM were thinned using standard electropolishing technique. Images were treated with ImageJ software [24]: the precipitate mean radius was estimated by averaging over more than 50 precipitates.

3. Experimental results

3.1. Microstructural characterization

The initial T6 state exhibited equiaxed grain structure, with grain size of approximatively 200 μm. These coarse and equiaxed grains are clearly due to full recrystallization of the rolled structure during the solutionizing treatment performed before the T6 treatment.

From this T6 state, the non-isothermal treatments have been chosen as in Bardel et al. [14] where a similar alloy was studied. An overview of the TEM experiments is presented in Fig. 3. All TEM observations were performed using a [001] Al zone axis.

In Fig. 3a, a sample in the T6 state was analyzed. As expected after such a treatment, very fine precipitates corresponding to the β'' phase were detected. These precipitates were found to be uniformly distributed in the aluminium matrix and to have an average radius of 1.6 nm.

After the *MT* treatment with $MT = 450$ °C, β'-rod-shaped precipitates were observed. They were found to be aligned along the three possible ⟨100⟩ directions of the aluminium matrix, as was reported in the literature for these precipitates [25]. In Fig. 3b, one family of β'-precipitates is viewed end-on. The mean radius of these precipitates is 4.6 nm.

After the *MT* treatment with $MT = 500$ °C, no β'-precipitates could be detected. During this treatment, the β'-precipitates were replaced by large incoherent precipitates associated with the equilibrium β-phase. These

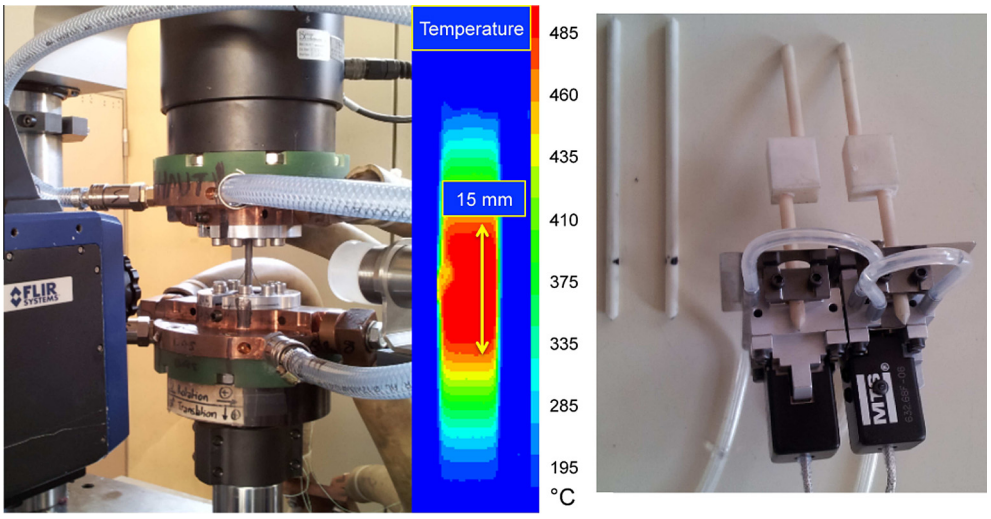

Fig. 2. Images of (a) the thermomechanical device during a temperature gradient measurement by infrared thermography and (b) the extensometer with modified alumine rods.

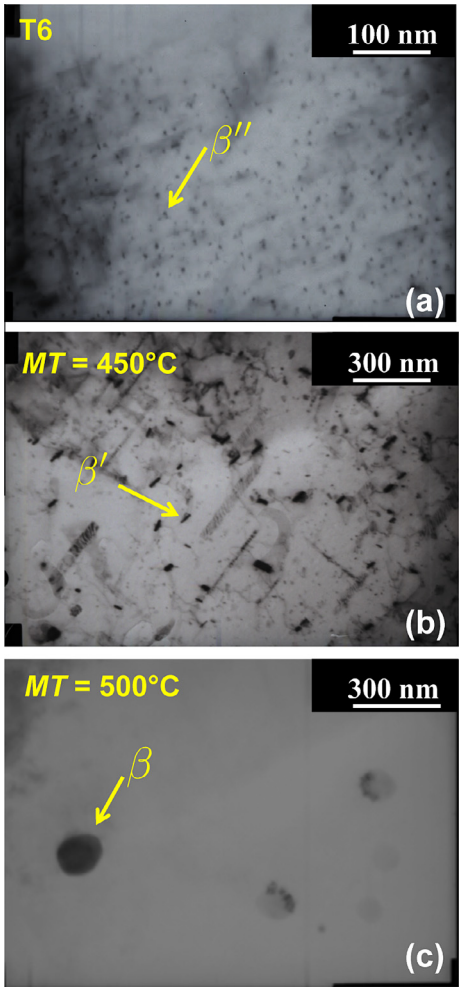

Fig. 3. TEM pictures for (a) T6 state, (b) sample heated to $MT = 450\,^{\circ}C$ and (c) $MT = 500\,^{\circ}C$. These observations validate the β' solvus temperature of $\approx 465\,^{\circ}C$ [26] used (as in Ref. [14]) for the simulation of precipitation.

precipitates do not contribute to the hardening and prevent nucleation of less stable $\beta'' - \beta'$ phases.

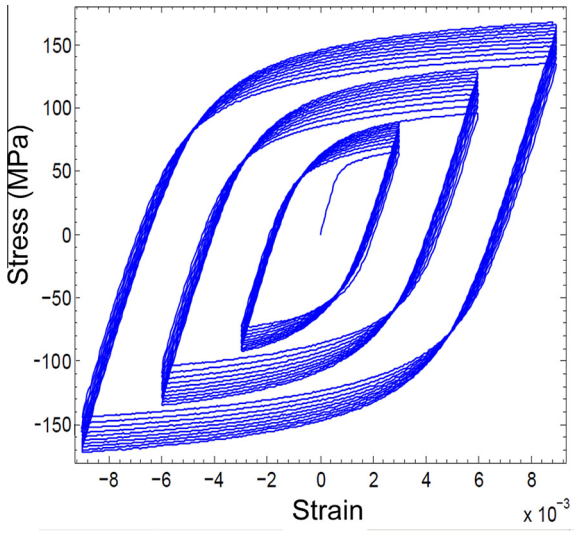

Fig. 4. Cyclic stress–strain curve for the MT treatment with $MT = 560\,^{\circ}C$. The evolution of the maximum stress amplitude shows a strong isotropic hardening.

It should be noted that these results are in agreement with the time–temperature–transformation diagram of the 6061 alloy determined by Massardier et al. [26]. Finally, these observations agree with the β' solvus temperature of $465\,^{\circ}C$ used (as in Ref. [14]) for the simulation of precipitation (see Section 4).

3.2. Elastoplastic behaviour

As shown in Fig. 1, the strain cycles were applied after non-isothermal heat treatments. As an example, a cyclic stress–strain curve for the MT treatment with $MT = 560\,^{\circ}C$ is shown in Fig. 4. The evolution of the maximum stress (reached during a cycle) shows a strong isotropic hardening for this sample.

Fig. 5 presents the evolution of the maximum stress with the cycle number. During these experiments, a wide variety

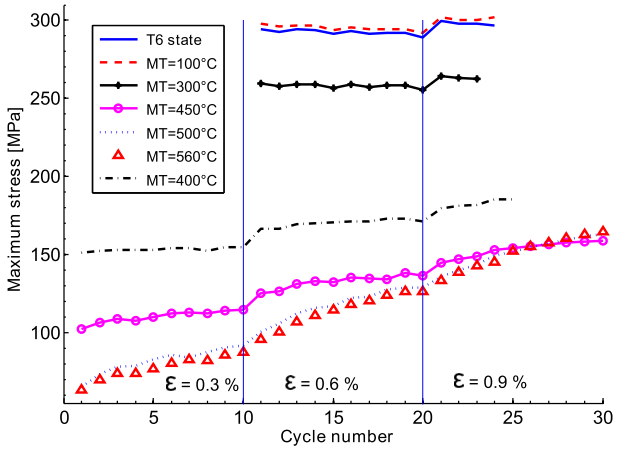

Fig. 5. Evolution of the maximum stress amplitude as function of the cycle number at T6 state and after thermal treatments characterized by various maximum temperatures (MT) and a fixed heating rate ($HR = 15°\ C\ s^{-1}$). Every 10 cycles (vertical line), the strain amplitude is increased. The first 10 cycles are purely elastic at T6 state and after $MT = 100\ °C$ and $MT = 300\ °C$ treatments. The increase of the maximum stress amplitude characterizes the isotropic hardening.

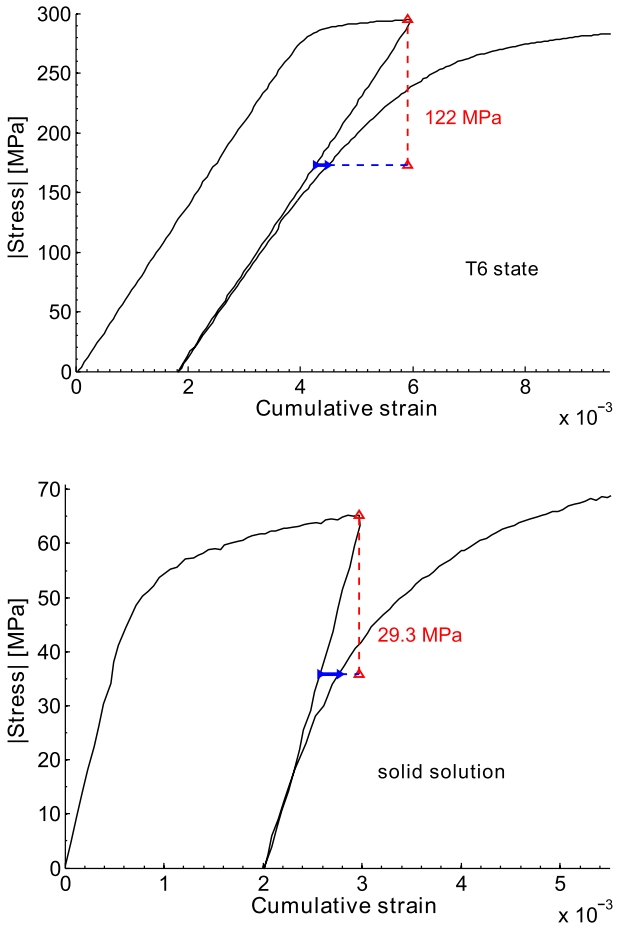

Fig. 6. Quantification of the Bauschinger effect (offset 0.02 %—horizontal blue segment) for the initial T6 state (upper figure) and when all hardening precipitates are dissolved (after a treatment characterized by $MT = 560\ °C$ and $HR = 15°\ C\ s^{-1}$) (lower figure). (For interpretation of the references to colour in this figure legend, the reader is referred to the web version of this article.)

of mechanical behaviour was obtained for the different heat treatments. The higher the maximum temperature, the lower the initial yield strength ($\sigma^{v}_{0.02\%}$).

The quantification of kinematic hardening requires the definition of a clear criterion to separate elastic from plastic domains. Kinematic hardening indeed depends on the plastic strain offset that is chosen. Therefore, in what follows, the offset of 0.02% is chosen. A larger offset would miss a large part of the hardening and a smaller offset would reach the detection limit of the extensometer.

Examples of reverse cycles are presented in Fig. 6 for the T6 state and a heat treatment characterized by $MT = 560\ °C$ and $HR = 15\ °C\ s^{-1}$ (no precipitate–solid solution). The T6 state obviously presents a larger Bauschinger effect, certainly due to the massive presence of precipitates. Note that, even for the precipitate-free state, the amplitude of the back-stress is not zero, which is in contradiction with what is assumed in several studies [12,10,11]. This Bauschinger effect has been observed for all cycles and thermal treatments.

We can see in Fig. 5 that the lower the precipitate density (increasing maximum temperature), the higher the cyclic hardening. Indeed, the T6 state as well as after thermal treatments with $MT = 100\ °C$ and $MT = 300\ °C$ exhibits a perfect kinematic behaviour (negligible isotropic hardening). The isotropic hardening component increases when the maximum temperature further increases, leading to a coarser precipitation state.

Thus, these cyclic curves highlight the strong effect of the precipitation state on: (i) the initial yield stress, (ii) the kinematic hardening component that increases with the density of precipitates and (iii) the isotropic hardening that increases when the precipitates dissolve and/or coarsen. This wide range of heat treatments will facilitate the modelling by providing separate information on both isotropic and kinematic hardening from the homogenized state to the fine T6 microstructure.

4. Modelling

4.1. Precipitate size distribution and volume fraction

The distribution of precipitates has been simulated for the MT and HR heat treatments using a recent implementation of a KWN model for $\beta'' - \beta'$ rods detailed in Bardel et al. [14]. In short, classical nucleation and growth theories (CNGTs) have been adapted to the precipitation of rod-shaped particles (number density N, tip radius r_p and length l), leading to:

$$\frac{dN}{dt} = N_0 Z \beta^* \exp\left[-\frac{\Delta G^*}{k_b T}\right]\left[1 - \exp\left(-\frac{t}{\tau}\right)\right] \quad (1)$$

$$\frac{dl}{dt} = 1.5\frac{D_{Mg}}{2r_p}\frac{X_{Mg} - X^i_{Mg}}{\alpha X^p_{Mg} - X^i_{Mg}} = 1.5\frac{D_{Si}}{2r_p}\frac{X_{Si} - X^i_{Si}}{\alpha X^p_{Si} - X^i_{Si}} \quad (2)$$

where N_0 is the nucleation site density, β^* is the condensation rate and Z is the Zeldovich factor, ΔG^* is the nucleation barrier, τ is the incubation time, X_{Mg} and X_{Si} are the matrix solute fraction; X^i_{Mg} and X^i_{Si} are the interfacial equilibrium solute fraction, X^p_{Mg} and X^p_{Si} are the precipitate solute fraction, and α is the ratio between matrix and precipitate mean atomic volume $v_{at}\left(\alpha = v^M_{at}/v^p_{at}\right)$. All these parameters have similar values as in Ref. [14].

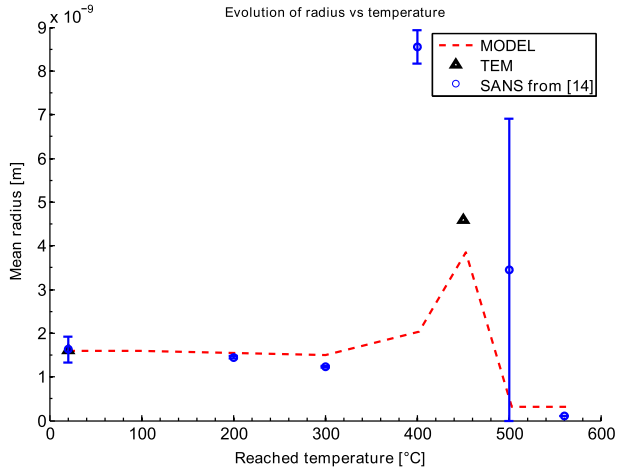

Fig. 7. Evolution of mean precipitate radius for T6 state (shown at $MT = 25\,^{\circ}C$) and thermal treatments with various maximum temperatures (MT). Small-angle neutron scattering data from Ref. [14] (in which a similar alloy was studied) are also reported for comparison.

The solubility product modified by the Gibbs–Thomson effect reads:

$$X^{i}_{\mathrm{Mg}}{}^{x} X^{i}_{\mathrm{Si}}{}^{y} = K_s \times \exp\left(\frac{r_0}{r}\right) \tag{3}$$

where r_0 is the capillarity length and K_s is the solubility product (expressed in atomic fraction and T in Kelvin):

$$\mathrm{Log}_{10} K_s = -\frac{A}{T} + B \tag{4}$$

Eqs. (1)–(3) were then integrated in a precipitation multi-class KWN-type model [27,15,16]. From a precipitate-free state (supersaturated solid solution), a T6 treatment (8 h at 175°C) has been applied. The calibration has been carried out by (i) adjusting the solubility product for the β'' – β' precipitates thanks to the dissolution temperature (738 K from Ref. [26]) and the precipitate volume fraction at the T6 state (1.6% as in Ref. [14]); then, (ii) fitting the interfacial energy to obtain the mean radius measured by TEM in the T6 state (cf. Fig. 3). For this particular alloy (cf. Table 1), $A = 20945$ K, $B = -28.7$ and $\gamma = 0.085$ J m^{-2} are obtained.[1] Fig. 7 shows that the proposed precipitation model gives an accurate description of precipitate mean radius for various treatments with maximum temperatures ranging from 200 to 560 °C.

4.2. Elastoplastic framework

In addition to the yield stress of pure aluminium σ_0, several contribution have been considered: an isotropic component R due to the interaction between dislocations and defects interactions and two kinematic contributions: X_G due to the pile-up of dislocations on grain boundaries and X_{ppt} due to the pile-up of dislocations around precipitates.

These contributions are introduced into a unified elastoplastic framework. For the sake of simplicity and according to the experiments, this paper is written in a unidirectional formalism. The additive partition of deformations (small strains) is assumed and the stress is expressed by Hooke's law of linear elasticity:

$$\sigma = E\left(\epsilon - \epsilon_p\right) \tag{5}$$

where ϵ and ϵ_p are the total and plastic strains, and E is the Young's modulus. A yield function f delimiting the elastic domain is introduced:

$$f(\sigma, X_G, X_{ppt}, R) = |\sigma - X_G - X_{ppt}| - (\sigma_0 + R) \tag{6}$$

In the elastic domain $f < 0$, and during plastic flow $f = 0$. The normality rule [23] provides the rate and direction of the plastic flow:

$$\dot{\epsilon_p} = \dot{\lambda}\frac{\partial f}{\partial \sigma} = \dot{\lambda} \times \mathrm{Sign}\left(\sigma - X_G - X_{ppt}\right) = \dot{\lambda} \times \mathrm{Sign}(\xi) \tag{7}$$

where $\xi = \sigma - X_G - X_{ppt}$ is the effective stress and $\dot{\lambda}$ (main unknown of the plastic problem) is the plastic multiplier, also defined as the norm of the plastic strain rate and then the cumulative plastic strain rate $\dot{\lambda} = |\dot{\epsilon_p}| = \dot{p}$. It is determined by the consistency condition $f = \dot{f} = 0$ during the flow [23], combined with Eqs. (5)–(7).

4.3. Initial yield stress

A microstructure-based yield stress model is used in this work. It takes the contribution of the whole precipitate size distribution into account, as well as the non-spherical shape of precipitates, their specific spatial distribution as well as competing shear and bypass strengthening mechanisms.

Indeed the yield stress of an aluminium alloy can be seen as the consequence of: (i) the Peierls friction and grain boundaries contributions included in σ_0, which is the yield stress of pure aluminium (≈10 MPa for a weak Hall–Petch effect) [2,6]; (ii) the solid-solution (SS) strengthening $\Delta\sigma_{SS} = k_j.C_j^{2/3}$ [28] where the concentrations C_j are provided by the precipitation model thanks to a balance between the initial content and precipitate volume fraction [14]; (iii) the forest term $\Delta\sigma_d$ that is usually negligible for an initial (undeformed) dislocation density [1,2,6]. In Starink et al.'s work [29] this assumption is validated for cold-rolled Al alloys and the contribution is estimated at 1.3 MPa; and (iv) the precipitate hardening effect $\Delta\sigma_p$ due to the distribution of precipitates.

These four contributions are homogenized in the slip planes thanks to a conventional power law, which depends on the difference in size and strength of obstacles [30]. This provides the macroscopic yield stress:

$$\sigma_y = \sigma_0 + R \tag{8}$$

where $R = \Delta\sigma_{SS} + \sqrt{\Delta\sigma_p^2 + \Delta\sigma_d^2}$ is the total isotropic contribution.

To calibrate this contribution on the experimental results the forest hardening is calculated as:

$$\Delta\sigma_d = M\alpha\mu b\sqrt{\rho} \tag{9}$$

where M is the Taylor factor, α is a constant ($\alpha = 0.27$ according to Ref. [31]), μ is the shear modulus of the aluminium, b is the Burgers vector and ρ is the dislocation density (initial value $\rho_0 = 10^{12}$ m^{-2} as in Ref. [10]).

A triangular network of precipitate obstacles (aligned along the [1 0 0] direction) is present in the {1 1 1} slip plane [32]. In a previous paper [14], two mechanisms were

[1] Note that these values are slightly different from those in Ref. [14] since the alloy composition in also different.

Table 2. Parameters of the yield stress model.

Parameter	Value	Sources
b [m]	2.86×10^{-10}	[35]
M	2	[31,1,5,6]
β	0.25	[9]
σ_0 [MPa]	≈10	[31]
E [GPa]	71.5	This work from T6
ν	≈0.33	[36]
r^c [nm]	1.6	This work by TEM
k_{Mg} [MPa/wt%$^{2/3}$]	23	Precipitate-free yield stress
k_{Si} [MPa/wt%$^{2/3}$]	23	Precipitate-free yield stress

introduced: shear (sh) and bypass (bp) according to the precipitate size. A quadratic homogenization law provides good results for various volume fractions and strengths of obstacles as explained in a dislocations dynamic study [33]. Then, we choose: $\Delta\sigma = \sqrt{\Delta\sigma^{sh^2} + \Delta\sigma^{bp^2}}$ [14,34], with:

$$\begin{cases} \Delta\sigma^{sh} = M(k\mu)^{3/2}\sqrt{\dfrac{\sum_{i<i_c} l_i N_i}{4\sqrt{3}\beta\mu b}}\left[\dfrac{\sum_{i<i_c} N_i r_i}{\sum_{i<i_c} N_i}\right]^{3/2} \\ \Delta\sigma^{bp} = \sqrt{2}M\beta\mu b\sqrt{\sum_{i>i_c} l_i N_i} \end{cases} \quad (10)$$

In these expressions $k = 2\beta b/r_c$ is deduced from the transition radius, which is supposed to be the mean radius of the T6 state [6,34]. The line tension constant β is chosen equal to 0.25 according to Brown et al. [9] and a lower bound of the mean Taylor factor is chosen $M = 2$ as in Refs. [1,31]. The distribution of precipitates is characterized by the radius r_i, the length l_i and the number density N_i of each class and the index i_c is the index of the shear/bypass transition radius.

The strengthening constants k_j of $\Delta\sigma_{SS}$ (for Mg and Si solutes) are fitted (cf. Table 2), as in Refs. [31,10], to reach the experimental yield stress when precipitates are dissolved ($MT = 560$ °C in Fig. 8).

Fig. 8 presents the resulting total yield strength for all MT and HR treatments, as well as for the T6 state. The yield strength resulting from the precipitation model coupled with the hardening model fits remarkably well the experimental values measured at the beginning of the first stress–strain cycle for all non-isothermal treatments. Note that this agreement, combined with the good predictions of the precipitation model (Fig. 7) gives us some confidence for the hardening model that will be introduced in the next section.

4.4. Isotropic hardening: the forest contribution

The classical Kocks–Meching–Estrin (KME) [19,18] dislocation evolution provides a simple framework to describe isotropic hardening due to dislocation interactions. It is based on a constitutive equation describing the evolution of the dislocation density ρ with strain:

$$\frac{\partial\rho}{\partial p} = M\left(k_1\sqrt{\rho} - k_2\rho\right) \quad (11)$$

where k_1 is related to the athermal work hardening limit and k_2 describes dynamic recovery. In parallel, a hardening equation (Eq. (9)) relates the dislocation density to the isotropic hardening.

This versatile framework has been improved by many authors to account for more and more complex systems and/or phenomena. Some important contributions will be discussed in the next paragraphs.

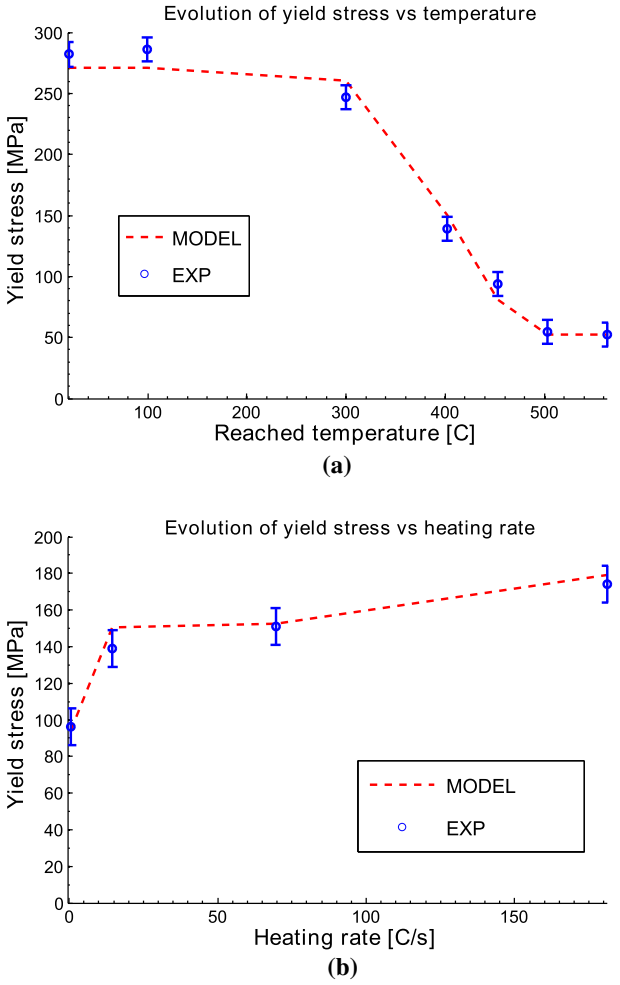

Fig. 8. Representation of the yield stress evolution given by the model (in red) for (a) the maximum temperature and (b) the heating rate studied.

4.4.1. Contribution of grain boundary dislocations

Sinclair et al. [13] proposed an adaptation of the KME formalism in order to account for the contribution of grain boundary dislocations. They added an additional term in Eq. (11) to describe the efficiency of dislocations stored at the boundary with respect to forest hardening. However, as this term is inversely proportional to mean grain diameter D, this contribution will be assumed negligible in the following since $1/D(\approx 10^4\ \mathrm{m}^{-1}) \ll \sqrt{\rho}(\approx 10^6\ \mathrm{m}^{-1})$ in our case.

4.4.2. Contribution of Orowan loops

First introduced by Estrin [18] and later improved by Simar et al. [6], the contribution of Orowan loops to hardening was expressed as an additional term $\varphi/(b\overline{L_{bp}})$ in Eq. (11), where φ is an efficiency term ranging from 0 to 1 and the distance $\overline{L_{bp}}$ is the mean distance between bypassed precipitates. This version is also used by Fribourg et al. [10] but in a different form where the dislocation density around precipitates is added to ρ in $\Delta\sigma_d$. The adaptation of Fribourg et al. for cyclic hardening in the presence of a distribution of precipitates provides $\rho_{ppt} = 2\pi\phi|n_{ppt}|N_{bp}\overline{R_{bp}}$, where $\overline{R_{bp}}$ and N_{bp} are the mean radius and the number density of bypassed precipitates.

However, the effect of the dislocation density stored as Orowan loops ρ_{ppt} is weak ($\rho \gg \rho_{ppt}$ in all simulated cases).

Moreover, the number of Orowan loops n_{ppt} stored around bypassed precipitates oscillates around zero when the sign of the plastic strain changes. Thus, the isotropic contribution proportional to $\sqrt{\rho_{ppt}}$ oscillates too. Such isotropic behaviour has not been observed experimentally and leads to the hypothesis that this isotropic contribution is a very small dynamic phenomenon and does not have to be taken into account.

4.4.3. Effect of precipitates on dynamic recovery constant k_2

In addition to the storage of Orowan loops, several authors [6,18] have noted that the presence of precipitates can modify the dynamic recovery constant k_2. Simar et al. [6] stated that the presence of Orowan loops increases the stress field around precipitates, favouring cross-slip, thus leading to an amplification of dynamic recovery. Using a Poisson process, Simar et al. [6] have shown that the probability of dynamic recovery without Orowan interference is $P(0) = \exp(-l_d\varphi/\overline{L_{bp}})$ with $l_d = 1/\sqrt{\rho}$:

$$k_2 = k_2^0 \times \exp\left(-\frac{\varphi l_d}{\overline{L_{bp}}}\right) + k_2^p \times \left[1 - \exp\left(-\frac{\varphi l_d}{\overline{L_{bp}}}\right)\right] \tag{12}$$

where $\overline{L_{bp}}$ is the mean distance between bypassed precipitates, which is computed from a given precipitate distribution by:

$$\overline{L_{bp}} = \sqrt{\frac{2}{\sum_{i>i_c} l_i N_i}} \tag{13}$$

with l_i and N_i are the length and the density of precipitates for the class "i" in the simulated distribution [14].

4.5. Grain boundaries contribution to kinematic hardening

From the microstructural analysis and in agreement with the literature, samples submitted to the MT treatment with $MT = 560\ ^\circ\mathrm{C}$ exhibit a microstructure where all $\beta'' - \beta'$ strengthening precipitates have been dissolved. However, as can be seen on the stress–strain cyclic curve of Fig. 4 and also in Fig. 5, there is obviously a kinematic component in the hardening of such sample. This kinematic hardening is assumed here to be due to grain boundaries, as described by Sinclair et al. [13] and also by Morrison et al. [37], even for grains as large as 300 μm. Indeed, the stress field developed by dislocations stopped at the grain boundary impedes the progress of similar dislocations and causes a backstress X_G. In the simple case where screening effects are negligible (small strain, i.e. no dislocation of opposite sign arriving in the same area on other slip systems or in adjacent grains), the backstress can be written as [13]:

$$X_G = M\frac{2\beta\mu b}{D}n_G \tag{14}$$

where D is the mean grain size (close to 200 μm here) and n_G is the average number of dislocations (of a given sign) blocked at the grain boundary on a given slip band. Note that n_G and X_G are considered here as signed variables: negative values mean a backstress in compression (when $\sigma < 0$). Following Sinclair et al. [13], the evolution of n_G with the plastic strain ϵ_p can be written as:

$$\frac{\partial n_G}{\partial \epsilon_p} = M\frac{\lambda_G}{b}\left[1 - \frac{n_G}{n_G^* \times \mathrm{Sign}(\dot{\epsilon_p})}\right] \tag{15}$$

where λ_G is the mean distance between slip lines in a shear band and the second term accounts for the finite number of sites available for dislocations at the boundary.

For this application, the contribution of Sinclair et al. [13] has been adapted to cyclic loading: the direction of loading has to be accounted for. Indeed, n_G converges to a positive n_G^* during forward loading, whereas it converges to a negative value during reverse loading. The term $n_G^* \times \mathrm{Sign}(\dot{\epsilon_p})$ in Eq. (15) accounts for this inversion of the backstress.

4.6. Precipitation effect on work hardening

Precipitation has an effect on kinematic hardening as shown, for example, by the experimental curves of Fig. 6. This component can be assessed from the precursor work of Ashby [8], and Brown and Stobbs [9]. Thanks to the Eshelby formalism [38,39], the unrelaxed plastic strain $\gamma_{ppt}^* = n_{ppt}b/2r$ due to the storage of n_{ppt} Orowan loops around spherical precipitates (of radius r) can be linked to the macroscopic kinematic stress X_{ppt} (the Orowan storage is a polarized mechanism [10]). Here, the geometry of precipitates (oriented in the $\langle 100\rangle$ direction) is assumed ellipsoidal and then the unrelaxed plastic strain is $\gamma_{ppt}^* = n_{ppt} \times b \times \sqrt{3}/l_{bp}$, where l_{bp} is the mean length of bypassed precipitates.

For a precipitate with the same shear modulus μ as the matrix [9], as detailed in the Appendix, the macroscopic kinematic stress X_{ppt} due to a volume fraction f_V^{bp} of bypassed precipitates is:

$$X_{ppt} = M\mu f_v^{bp}\Omega\gamma_{ppt}^* = M2\mu f_v^{bp}\Omega \times \epsilon_{ppt}^* \tag{16}$$

where $\Omega = (7 - 5\nu)/15(1 - \nu)$ [9,40] (for spherical precipitates) is the accommodation factor. In the case of ellipsoids ($a_1 = \kappa a_2 > a_2 = a_3$), Ω is deduced from Mura's contribution [40]:

$$\begin{aligned}\Omega = 1 - 2S_{3131} = {} & (2 - 2\nu)^{-1}\left(\kappa^2 - 1\right)^{-5/2} \\ & \times \left[\mathrm{acosh}(\kappa)\left(\kappa^3(1 + \nu) + \kappa(2 - \nu)\right)\right. \\ & \left. + \sqrt{\kappa^2 - 1}\left(\kappa^4(1 - \nu) + \kappa^2(\nu - 4)\right)\right]\end{aligned} \tag{17}$$

This expression is quite different from the one of Proudhon et al. [7] and Fribourg et al. [10], where $\Omega = 1$ and the Young's modulus is used rather than the shear modulus. Moreover, when the shear modulus μ^* of the precipitates is different from the one of the matrix (available data for the closest precipitate, Mg_2Si, yields $\mu^* = 46.4$ GPa [4]), the Eshelby inhomogeneity problem leads to [40]:

$$X_{ppt} = M \times \frac{\mu \times \Omega \times \mu^* \times b \times \sqrt{3}}{\mu^* - \Omega(\mu^* - \mu)}\frac{f_v^{bp}}{l_{bp}}\varphi n_{ppt} = \chi\frac{f_v^{bp}}{l_{bp}}n_{ppt} \tag{18}$$

where χ is a constant and $\varphi \in [0, 1]$ has been introduced by Simar et al. [6] to adjust the efficiency of the Orowan loops.

Next, in order to quantify the evolution of kinematic hardening in Eq. (18), the number of Orowan loops n_{ppt} stored around precipitates must be expressed as a function of plastic strain. In Proudhon et al. [7], a reasoning close to the one of Sinclair et al. [13] led to an equation similar to Eq. (15) with a maximum number of Orowan loops n_{ppt}^*. Adapting this expression to cyclic tests, the evolution of

the number of dislocations stored around precipitates can be written as:

$$\frac{\partial n_{ppt}}{\partial \epsilon_p} = M\frac{l_{bp}}{b\sqrt{3}}\left[1 - \frac{n_{ppt}}{n^*_{ppt} \times \mathrm{Sign}(\dot{\epsilon_p})}\right] \tag{19}$$

Precipitation affects the kinematic hardening but also the isotropic contribution as highlighted in Fig. 5. These effects are included in Eqs. (8) and (12). We recall here that the effect of stored dislocations (as Orowan loops) on forest hardening (ρ_{ppt}) has been neglected (see justification in previous section).

5. Numerical integration and calibration

5.1. Numerical integration

The material behavior is first integrated using an elastic computation where the input is the experimental strain. This step is acceptable if the yield surface is $f \leqslant 0$, otherwise the integration of the plastic problem is performed under the consistency condition. The implementation has been introduced in the PreciSo precipitation software [15,34] to benefit from a full coupling between microstructural and mechanical evolutions.

In order to facilitate the resolution, an explicit time integration form is used thanks to an adaptive RK45 algorithm (implemented as in Ref. [41]) that solves the following differential system:

$$\begin{cases} \dot{\sigma} = E\left[\dot{\epsilon} - \dot{\lambda} \times \mathrm{Sign}(\xi)\right] \\ \dot{\rho} = M\left[k_1\sqrt{\rho} - k_2\rho\right]\dot{\lambda} \\ \dot{n}_G = \frac{M\lambda_G}{b}\left[\mathrm{Sign}(\xi) - \frac{n_G}{n^*_G}\right]\dot{\lambda} \\ \dot{X}_G = \frac{2M^2\lambda_G\beta\mu}{D}\left[\mathrm{Sign}(\xi) - \frac{n_G}{n^*_G}\right]\dot{\lambda} \\ \dot{n}_{ppt} = \frac{Ml_{bp}}{b\sqrt{3}}\left[\mathrm{Sign}(\xi) - \frac{n_{ppt}}{n^*_{ppt}}\right]\dot{\lambda} \\ \dot{X}_{ppt} = \chi\frac{Mf_v^{bp}}{b\sqrt{3}}\left[\mathrm{Sign}(\xi) - \frac{n_{ppt}}{n^*_{ppt}}\right]\dot{\lambda} \\ \Delta\dot{\sigma}_d = \frac{M\alpha\mu b}{2\sqrt{\rho}}\dot{\rho} \\ \dot{R} = \frac{\Delta\sigma_d\Delta\dot{\sigma}_d}{\sqrt{\Delta\sigma_p^2+\Delta\sigma_d^2}} \end{cases} \tag{20}$$

This system is solved by recalling that $\dot{\epsilon_p} \times \mathrm{Sign}(\xi) = \dot{\lambda}$ and $\partial|n_{ppt}|/\partial t = \dot{n}_{ppt} \times \mathrm{Sign}(n_{ppt})$ and under the hypothesis that the dynamic precipitation and the grain size evolution due to strain can be neglected ($\dot{D}, \Delta\dot{\sigma}_{SS}, \Delta\dot{\sigma}_p, \dot{N}_{bp}\ldots$ equal to zero). Note that more complex forms can be found in Ref. [34].

Table 3. Parameters used for the plastic modeling.

Parameter	Value	Sources
k_1 [m^{-1}]	87×10^6	Fitted on $MT = 560$ °C
k_2^0	3.5	Fitted on $MT = 560$ °C
k_2^p	0.25	Fitted on isotropic evolution
D [μm]	200	Metallography
λ_G [μm]	25.8	Fitted on $MT = 560$ °C
n^*_G	1100	Fitted on $MT = 560$ °C
E [GPa]	71.5	Fitted on T6
ν	0.33	[36]
μ^* [GPa]	46.4	Mg_2Si (closest precipitate) [4]
α	0.27	[31]
ρ_0 [m/m^3]	1×10^{12}	[10]
φ	1	[18]
n^*_{ppt}	$\to \infty$	No saturation

The main unknown of this problem is the plastic multiplier $\dot{\lambda}$, which is deduced from the consistency condition $f = \dot{f} = 0$ [23] and updated at each time step:

$$\dot{\lambda} = \frac{\mathrm{Sign}(\xi)E\dot{\epsilon}}{\left(E + \frac{\dot{R}}{\dot{\lambda}} + \mathrm{Sign}(\xi)\left[\frac{\dot{X}_G}{\dot{\lambda}} + \frac{\dot{X}_{ppt}}{\dot{\lambda}}\right]\right)} \tag{21}$$

5.2. Calibration

There are several parameters in the differential system of Eqs. (20) (all parameters are recalled in Table 3). Experimental cyclic tests allow a simple identification in three stages:

5.2.1. Yield stress

Most of the parameters ($b, M, \beta, \sigma_0, E, \nu, r^c, k_{Mg}$ and k_{Si}) have been identified on the yield stress evolution as in Ref. [14] (cf. Fig. 8 and Table 2). Note that the line tension constant $\beta = 0.25$ has been chosen as in Ref. [9]. The same order of magnitude can be found in a recent dislocation dynamic (DD) study [42] and in Brown et al. [9]. This value is assumed constant here although some fluctuations may exist with the evolution of dislocation characteristics [42]. Finally, the mean Taylor factor has been chosen as $M = 2$ as in Refs. [31,1]. This value might seem quite far from what is conventionally given by the Taylor's model ($\approx$3) but this model assumes random texture and a constant resolved shear stress for all the slip systems. These conditions are probably not respected here, especially if precipitates induce cross-slip. Note that this value can also be affected by the type of mixture law that is used (see DD simulations in Ref. [33]).

5.2.2. Precipitate-free state

The constants k_1, k_2^0, λ_G and n^*_G have been determined (cf. Table 2) from the precipitate-free state after the $MT = 560$ °C treatment. Indeed, for a constant strain amplitude, each increment of stress and associated saturation can be correlated to the isotropic hardening (k_1 and k_2^0).

Kinematic hardening is generally attributed to precipitates in age-hardening aluminium alloys. However, it was necessary to introduce a grain boundary contribution X_G in order to reproduce the Bauschinger effect for the precipitate-free $MT = 560$ °C sample. The constants n^*_G and λ_G have been fitted so that the Bauschinger effect could be

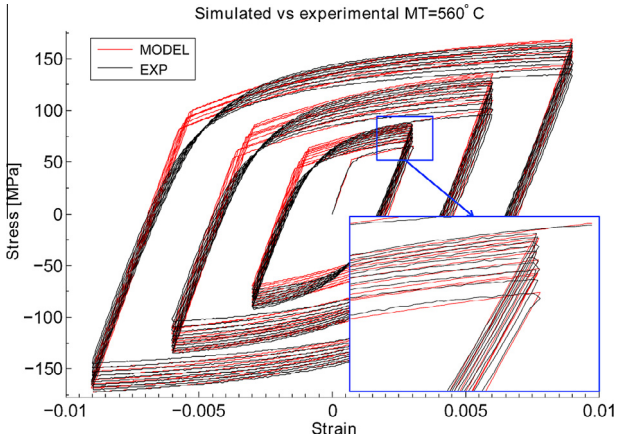

Fig. 9. Comparison between experimental and modelled stress–strain curves after the MT treatment with $MT = 560$ °C (where all precipitates are dissolved).

observed for all cycles and amplitudes. The maximum number of dislocation per slip band needed to fit the experiments is much higher than in Sinclair et al. [13] on copper (1100 vs. 6.7). Nevertheless, the ratios $n_G^* b/\lambda_G \approx 12 \times 10^{-3}$ that represent the maximum plastic shear angle in each slip band have a similar order of magnitude ($\approx 5 \times 10^{-3}$ in Ref. [13]). Fig. 9 shows the results of the fitting procedure on the samples where all precipitates are dissolved ($MT = 560\ ^\circ$C).

5.2.3. Precipitated states

The precipitate effect has then been introduced by fitting k_2^p, φ and n_{ppt}^* to limit the isotropic hardening for the coarse

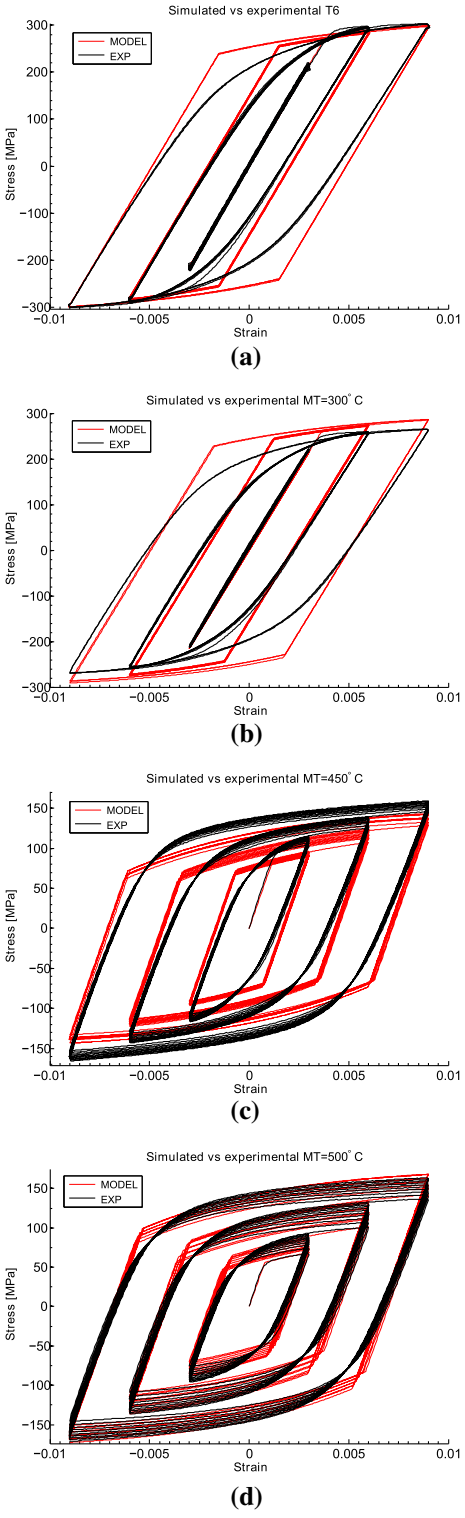

Fig. 10. Comparison between simulations and experimentations for maximum temperature (MT) tests (with heating rate $HR = 15^\circ$ C s$^-$): (a) T6 state; (b) $MT = 300^\circ$ C s$^-$; (c) $MT = 450^\circ$ C s^{-1}; (d) $MT = 500\ ^\circ$C/s.

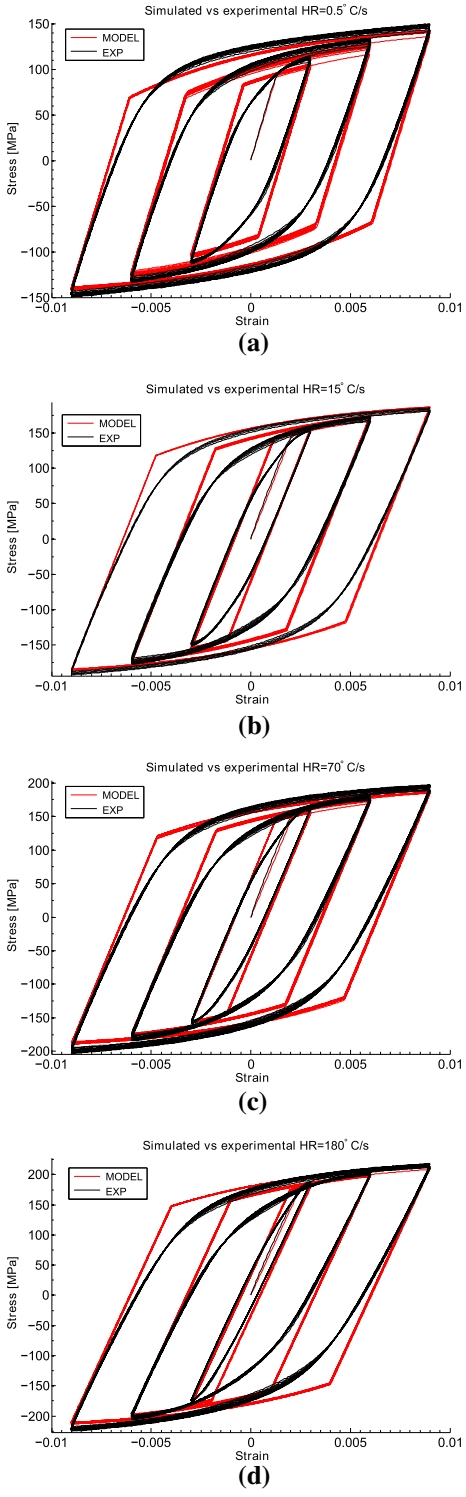

Fig. 11. Comparison between simulations and experimentations for heating rate (HR) tests (with maximum temperature $MT = 400\ ^\circ$C): (a) $HR = 0.5^\circ$ C s^{-1}; (b) $HR = 15^\circ$ C s^{1-}; (c) $HR = 70^\circ$ C s^{-1}; (d) $HR = 180^\circ$ C s^{-1}.

bypassed states and to increase the kinematic contribution on curves where the precipitate density is high. In all the simulations presented in Figs. 10 and 11 the storage of Orowan loops (associated with n_{ppt} dislocations) predicted by the modified version of Proudhon's relation (19) is very small (close to a few MPa) irrespective of the saturation value n^*_{ppt} and φ. Thus, in order to decrease the number of fitting parameters, the choice was made to keep an ideal storage case $\varphi = 1$ (as in Ref. [18]) and no saturation in the n_{ppt} evolution ($n^*_{ppt} \to \infty$). The numerical value X_{ppt} is still small and the Bauschinger effect (offset 0.02%) is still underestimated in the first stage of the plastic flow for several samples, despite a consistent hardening slope after the elastoplastic transition. Our fitting provides $k_2^p < k_2^0$, which suggests that precipitates rather pin the dislocations than favour cross-slip, as already proposed in Ref. [18] (this effect is probably due to the shearing of precipitates by block dislocations).

6. Results and discussion

6.1. Yield stress, kinematic and isotropic hardening

Fig. 10 compares the experimental stress–strain cyclic curves and the one predicted by the system of Eqs. (20) for all investigated *MT* treatments. It can be seen that both kinematic and isotropic hardening are well captured by the model: the fully precipitated T6 state exhibits high yield stress and a constant isotropic hardening (superimposed cyclic curves), whereas the precipitate-free state exhibits low yield stress and important isotropic hardening. Similar observations can be done in Fig. 11, which compares simulations and experiments for various *HR* treatments. Generally speaking, Figs. 10 and 11 show that the higher the precipitate density, the higher the kinematic hardening.

6.2. The role of hardening components

Thanks to this approach, it is now possible to differentiate the contributions of hardening and plastic flow. Fig. 12 describes all contributions of isotropic hardening (dislocations, precipitates and solid solution) and kinematic hardening (grain boundaries and precipitates) to the total flow stress for all *MT* treatments (a) and for $MT = 560\ ^\circ C$ as a function of the cycle number. It can be noted that under 400 °C, precipitation is the major source of hardening, even after the last deformation cycle (see Fig. 12a). Moreover, for the $MT = 560\ ^\circ C$ treatment, dislocation hardening takes more and more importance as deformation increases (see Fig. 12b).

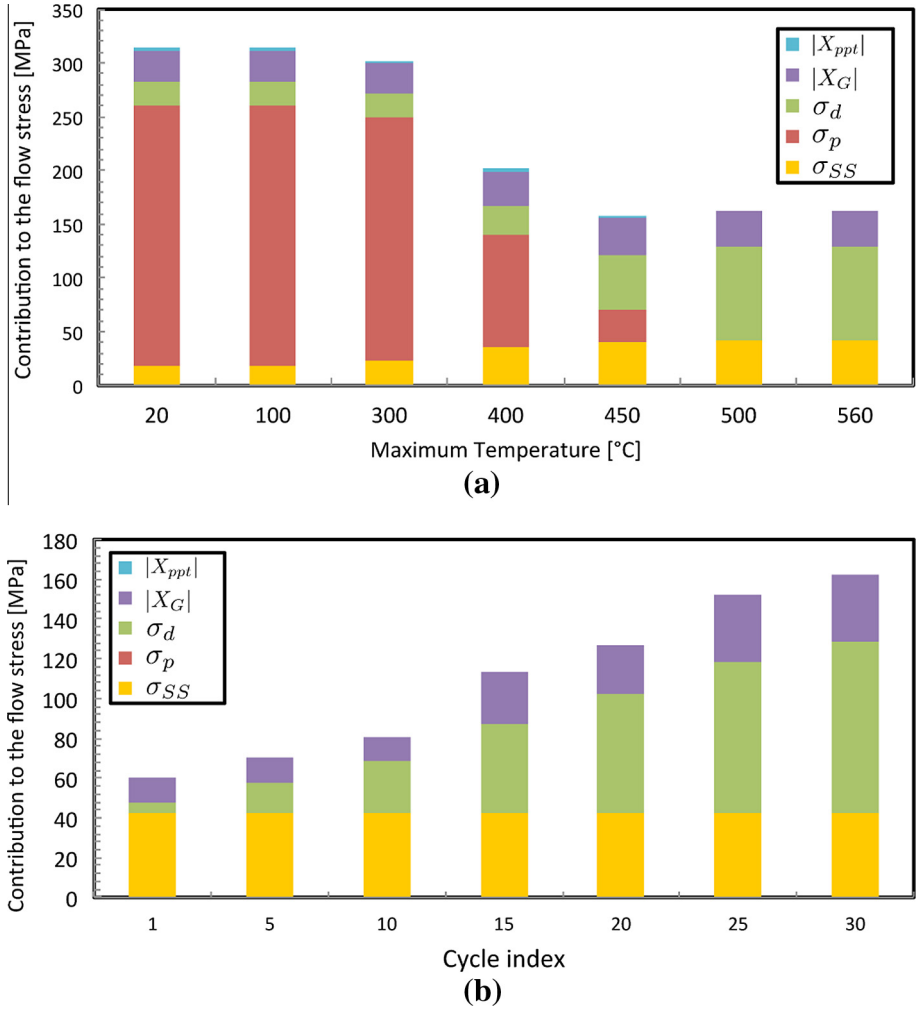

Fig. 12. Contributions to the flow stress: (a) at the end of the last deformation cycle at 0.9% for all *MT* treatments; (b) for the $MT = 560\ ^\circ C$ treatment as a function of the cycle number.

6.3. Elastoplastic transition

However, though yield stress and hardening are well described by the model, the elastoplastic transition occurring after the first cycle requires further effort to achieve an accurate representation. Nevertheless, as shown for example in the T6 state (Fig. 10a), the kinematic hardening stored during the first tensile loading is much lower than the experimental Bauschinger effect (offset 0.02%) observed in the following compressive test. This effect is due to the slip irreversibility phenomena already mentioned in Refs. [10,12,43]. With a classical version of the kinematic hardening this effect cannot be modelled because by increasing the backstress as in the experiments the hardening slope would become too high compared to experimental one. To improve this version a larger backstress in the elastoplastic transient is needed. According to Fribourg et al. [10] and Han et al. [12], this effect can be induced by the Orowan loops that mask the precipitates during the first step of the reverse loading, but here the number of Orowan loops is low (small strain). Then, the present effect is quite probably induced by the slip irreversibility due to sheared precipitates as reported in Ref. [43].

6.4. Grain size effect

This coupled model opens new prospects to study the effect of grain size on kinematic hardening. As highlighted in Ref. [37], the grain size has a potential impact on the presence of persistent slip band morphologies and then probably on λ_G, which is assumed constant as in Sinclair et al. [13].

6.5. Connection to the Armstrong–Frederick model

A simple unidirectional and physically based formalism has been proposed in this paper. It is remarkable that this formalism is rigorously equivalent to the widely used Armstrong–Frederick phenomenological law (see Eq. (23) of Ref. [23]):

$$\dot{X} = C^{AF}\dot{\epsilon}_p - \gamma^{AF}X\dot{p} \tag{22}$$

where C^{AF} and γ^{AF} are two phenomenological constants. Indeed, thanks to Eqs. (20), this work reveals the physical meaning of the phenomenological constants C^{AF} and γ^{AF} that can be identified as $C_G^{AF} = 2M^2\beta\mu\lambda_G/D$ and $\gamma_G^{AF} = M\lambda_G/(bn_G^*)$ for the grain boundary contribution and $C_{ppt}^{AF} = \chi f_V^{bp}M/(b\sqrt{3})$ and $\gamma_{ppt}^{AF} = Ml_{bp}/(b\sqrt{3}n_{ppt}^*)$ for the precipitate contribution. Thus, this model can be straightforwardly written in the Armstrong–Frederick tensorial form, while keeping its physical bases. To the authors' knowledge, such a connection had never been proposed before.

7. Conclusion

Aluminium 6061-T6 samples were subjected to a wide range of non-isothermal heat treatments leading to various microstructural state from T6 to fully dissolved precipitate-free state. These two extreme states were investigated by TEM.

All samples were then subjected to multilevel cyclic loading, highlighting the complex behaviour of this age-hardening alloy at room temperature for different precipitation states. For the T6 state, a high initial yield stress with a behaviour similar to a pure kinematic behaviour is observed (the isotropic contribution to the yield stress is constant during the cycles). For other treatments, the fewer the precipitates, the lower is the initial yield stress and the higher is isotropic hardening.

A recently developed precipitation model, particularly adapted to these precipitates, has been used to predict the precipitation state (in terms of the full precipitation size distribution) for each non-isothermal treatment. This model was then coupled to a strengthening model in order to predict the yield stress. This coupling was validated comparing the experimental and predicted yield stress for various precipitation states.

A specific effort was devoted to build a novel work-hardening model based on the KME formalism. In addition to the classical forest isotropic hardening, this model considers the effect of both grain boundaries and precipitates on kinematic hardening as well as their effect on the isotropic contribution. Several parameters were identified thanks to cyclic tests performed on the two extreme conditions: fully precipitated and precipitate-free states. This model gives a good agreement for both isotropic and kinematic hardening.

The coupling between the precipitation, yield stress and hardening models provides a powerful and versatile framework able to predict and/or analyze cyclic tests for a wide range of microstructural states.

Moreover, this model provides a physical meaning for the constants of the tensorial Armstrong–Frederick law as far as the grain boundaries and precipitate contributions are concerned.

Acknowledgements

The authors gratefully acknowledge AREVA and the French Atomic Energy Commission (CEA) for industrial and financial support, particularly F. Bourlier and J. Garnier. A. Deschamps and T. Chaise are also thanked for fruitful discussions. The authors are grateful to the CLYME (Consortium Lyonnais de Microscopie Electronique) for access to 200CX microscope. The "Life extension and manufacturing processes" teaching and research Chair sponsored by AREVA and SAFRAN is also gratefully acknowledged for partial financing support.

Appendix A.

The introduction of a strained ellipsoidal inclusion in the crystal (assumed elastic) is an Eshelby problem [9]. For small perturbations, the partition of strains $\epsilon_{ij} = \epsilon_{ij}^e + \epsilon_{ij}^*$ leads to [40]:

$$\sigma_{ij} = 2\mu\left(\epsilon_{ij} - \epsilon_{ij}^*\right) + \lambda\delta_{kl}\left(\epsilon_{kl} - \epsilon_{kl}^*\right) \tag{23}$$

where the total strain is $\epsilon_{ij} = S_{ijkl}\epsilon_{kl}^*$ with S_{ijkl} being the Eshelby tensor. Applying this relation in the slip plane $\epsilon_{13} = \epsilon_{31} = \epsilon_{ppt}^*$ as in Ref. [9], we get a scalar expression:

$$\sigma_{31} = 2\mu\left(S_{31kl}\epsilon_{kl}^* - \epsilon_{31}^*\right) \tag{24}$$

where only ϵ_{13} and ϵ_{31} are not equal to zero in the slip plane. By symmetry $S_{ijkl} = S_{jikl} = S_{ijlk}$, leading to:

$$\sigma_{31} = 2\mu(2S_{3131} - 1) = -2\mu\Omega\epsilon_{31}^* = -\mu\Omega\gamma_{31}^* \tag{25}$$

where $\Omega > 0$ is the accommodation factor.

References

[1] A. Simar, Y. Bréchet, B. de Meester, A. Denquin, C. Gallais, T. Pardoen, Prog. Mater. Sci. 57 (2012) 95.
[2] O. Myhr, O. Grong, S. Andersen, Acta Mater. 49 (2001) 65.
[3] O. Myhr, O. Grong, H. Fjaer, C. Marioara, Acta Mater. 52 (2004) 4997.
[4] X. Wang, W. Poole, S. Esmaeili, D. Lloyd, J. Embury, Metal. Mater. Trans. A 34 (2003) 2913.
[5] C. Gallais, A. Denquina, Y. Bréchet, G. Lapasset, Mater. Sci. Eng. A 496 (2008) 77.
[6] A. Simar, Y. Bréchet, B. de Meester, A. Denquin, T. Pardoen, Acta Mater. 55 (2007) 6133.
[7] H. Proudhon, W. Poole, X. Wang, Y. Bréchet, Philos. Mag. 88 (2008) 621.
[8] M. Ashby, Philos. Mag. 14 (1966) 1157.
[9] L. Brown, W. Stobbs, Philos. Mag. 23 (1971) 1185.
[10] G. Fribourg, Y. Bréchet, A. Deschamps, A. Simar, Acta Mater. 59 (2011) 3621.
[11] J. da Costa Teixeira, L. Bourgeois, C. Sinclair, C. Hutchinson, Acta Mater. 57 (2009) 6075.
[12] W. Han, A. Vinogradov, C. Hutchinson, Acta Mater. 59 (2011) 3720.
[13] C. Sinclair, W. Poole, Y. Bréchet, Scripta Mater. 55 (2006) 739.
[14] D. Bardel, M. Perez, D. Nelias, A. Deschamps, C. Hutchinson, D. Maisonnette, et al., Acta Mater. 62 (2014) 129.
[15] M. Perez, M. Dumont, D. Acevedo-Reyes, Acta Mater. 56 (2008) 2119.
[16] M. Perez, M. Dumont, D. Acevedo-Reyes, Acta Mater. 57 (2009) 1318.
[17] H. Mecking, U. Kocks, Acta Metal. 29 (1981) 1865.
[18] Y. Estrin, Unified Constitutive Laws of Plastic Deformation, Chapter Dislocation-Density-Related Constitutive Modeling, Academic Press, 1996.
[19] U. Kocks, H. Mecking, Prog. Mater. Sci. 48 (2003) 171.
[20] D. Maisonnette, M. Suery, D. Nelias, P. Chaudet, T. Epicier, Mater. Sci. Eng. A 528 (2011) 2718.
[21] S. Esmaeili, D. Lloyd, W. Poole, Acta Mater. 51 (2003) 3467.
[22] M. Coret, S. Calloch, A. Combescure, Int. J. Plast. 18 (2002) 1707.
[23] J. Chaboche, Int. J. Plast. 24 (2008) 1642.
[24] C.A. Schneider, W.S. Rasband, K.W. Eliceiri, Nat. Methods 9 (2012) 671.
[25] M. Jacobs, Phil. Mag. (1972) 26.
[26] V. Massardier, T. Epicier, P. Merle, Acta Mater. 48 (2000) 2911.
[27] R. Wagner, R. Kampmann, Materials science and technology: a comprehensive treatment, Chapter Homogeneous second phase precipitation, vol. 5, John Wiley & Sons Inc, 1991, 213p.
[28] J. Friedel, Dislocations, Pergamon Press, 1964.
[29] M. Starink, A. Deschamps, S. Wang, Scr. Mater. 58 (2008) 377.
[30] U. Kocks, A. Argon, M. Ashby, Prog. Mater. Sci. 19 (1975) 1.
[31] A. Deschamps, Y. Bréchet, Acta Mater. 47 (1999) 293.
[32] S. Esmaeili, D. Lloyd, W. Poole, Acta Mater. 51 (2003) 2243.
[33] S. Queyreau, G. Monnet, B. Devincre, Acta Mater. 58 (2010) 5586.
[34] D. Bardel, Role de la microstructure d'un alliage a durcissement structural sur son comportement et sa tenue mecanique sous sollicitations cycliques apres un transitoire thermique (Ph.D. thesis), INSA Lyon, 2014.
[35] C. Ravi, C. Wolverton, Acta Mater. 52 (2004) 4213.
[36] S. Sharma, Metal. Mater. Trans. A 31A (2000) 773.
[37] D.J. Morrison, J.C. Moosbrugger, Int. J. Fatigue 19 (1997) 51.
[38] J. Eshelby, Proc. R. Soc. 241 (1957) 376.
[39] J. Eshelby, Proc. R. Soc. 252 (1959) 561.
[40] T. Mura, Micromechanics of Defects in Solids, Martinus Nijhoff publishers, 1987.
[41] E. Hairer, S. Norsett, G. Wanner, Solving Ordinary Differential Equations I (Non Stiff Problems), Springer, 1993.
[42] S. Queyreau, B. Devincre, Philos. Mag. Lett. 89 (2009) 419.
[43] A. Deschamps, B. Decreus, F.D. Geuser, T. Dorin, M. Weyland, Acta Mater. 61 (2013) 4010.